



HAL
open science

Capillary, viscous, and geometrical effects on the buckling of power-law fluid filaments under compression stresses

Anselmo Soeiro Pereira, Aurélien Larcher, Elie Hachem, Rudy Valette

► **To cite this version:**

Anselmo Soeiro Pereira, Aurélien Larcher, Elie Hachem, Rudy Valette. Capillary, viscous, and geometrical effects on the buckling of power-law fluid filaments under compression stresses. *Computers and Fluids*, 2019, 190, pp.514-519. 10.1016/j.compfluid.2019.06.014 . hal-02428734

HAL Id: hal-02428734

<https://hal.science/hal-02428734>

Submitted on 25 Oct 2021

HAL is a multi-disciplinary open access archive for the deposit and dissemination of scientific research documents, whether they are published or not. The documents may come from teaching and research institutions in France or abroad, or from public or private research centers.

L'archive ouverte pluridisciplinaire **HAL**, est destinée au dépôt et à la diffusion de documents scientifiques de niveau recherche, publiés ou non, émanant des établissements d'enseignement et de recherche français ou étrangers, des laboratoires publics ou privés.



Distributed under a Creative Commons Attribution - NonCommercial 4.0 International License

Capillary, viscous, and geometrical effects on the buckling of power-law fluid filaments under compression stresses

Anselmo Pereira^a, Aurélien Larcher^a, Elie Hachem^a,
Rudy Valette^a

^a*MINES ParisTech, PSL Research University, Centre de Mise en Forme des
Matériaux (CEMEF), CNRS UMR 7635, CS 10207 rue Claude Daunesse, 06904
Sophia-Antipolis, France.*

Abstract

Thanks to an adaptive variational multi-scale method for multiphase flows with surface tension, we investigate through direct numerical simulations and scaling laws the buckling of filaments of power-law fluids compressed at a constant velocity by two parallel pistons. Under low gravity (the Laplace pressure exceeds the hydrostatic pressure) and inertial conditions (very small Reynolds numbers), two regimes are observed for slender filaments: a first one driven by the capillary force and during which there is no deflection; and a second folding regime that is dominated by the compressive viscous force. The transition between these two scenarios is given by a critical capillary number, which in turn appears as an increasing function of the flow behaviour index. Our main results are summarised in two-dimensional phase diagrams whose axes are a slenderness parameter and the capillary number.

Key words: buckling instability, power-law fluid, compression, direct numerical simulation

1 Introduction

Under compression stresses, free liquid filaments and/or jets develop some of the most fascinating instabilities in fluid mechanics: the buckling ones (Barnes and Woodcock, 1958). Beyond a critical axial load, [slender viscous fluid filaments](#) tend to buckle, as the energy related to the buckling deformation becomes smaller than the cost of compression (Taylor, 1969; Cruickshank, 1988; Yarin and Tchavdarov, 1996; Mahadevan et al., 1998, 2000). For small Newtonian fluid filaments compressed at a very small Reynolds number (negligible inertial force), for instance, the folding deformation emerges from a competition between geometrical, surface tension and viscous effects (Le Merrier et al., 2012). In addition, Newtonian viscous jet columns can bend, twist and stretch when hitting a surface or a substrate at higher Reynolds numbers, following the balance between viscous, gravitational, and inertial forces (Ribe, 2003; Ribe et al., 2006, 2012). Such instabilities are observed in a variety of contexts, which includes glass plate fabrication (Pilkington, 1969), [polymer processing](#) (Pearson, 1985), and folding of geological structures (Griffiths and Turner, 1988; Johnson and Fletcher, 1994).

Typically, in industry, the buckling instability represents a major source of irregularities for container-filling processes related to non-Newtonian fluids. More specifically, during these processes, the superposition of several coils, consecutively formed as a result of the fluid filament compression, originates

Email addresses: anselmo.soeiro.pereira@mines-paristech.fr (Anselmo Pereira), aurelien.larcher@mines-paristech.fr (Aurélien Larcher), elie.hachem@mines-paristech.fr (Elie Hachem), rudy.valette@mines-paristech.fr (Rudy Valette).

a helical fluid column, the centre of which is filled with air. Later on, this column eventually collapses, entraining a significant amount of air towards the fluid substrate and compromising the quality of the final product. Understanding and controlling the buckling instabilities when dealing with this kind of processes is then crucial. Despite some recent and significant works regarding these instabilities in Newtonian scenarios (Le Merrer et al., 2012; Habibi et al., 2014; Ribe, 2017), many aspects of the problem remain unclear, such as the effects of non-Newtonian signatures (pseudoplasticity, dilatancy, thixotropy, yield stress etc.) on them (Tomé et al., 2019).

In the present work, we study the buckling of pseudoplastic, Newtonian and dilatant fluid filaments, of which viscosity is given by a power-law constitutive equation (Ostwald, 1925; Bird et al., 1987). The filaments are compressed at a constant velocity by two parallel pistons, under both low gravity and low inertia conditions. Following the compression process, the fluid deflection is carefully analysed thanks to an adaptive variational multi-scale method for three materials (air, non-Newtonian fluid, and pistons), with surface tension, combined with a level-set function to provide a precise position of the phase interfaces. Different deformation regimes are observed and explored in the light of scaling laws. As a result, buckling criteria based on geometrical, surface tension and non-Newtonian viscous effects are presented and discussed.

The organization of the paper is as follows. The description of the physical formulation and numerical method is presented in Sections 2 and 3. Our main results are discussed in Section 4, where the buckling of non-Newtonian fluid filaments is analysed and [summarised](#) in two-dimensional phase diagrams. Finally, conclusions are drawn in the closing section.

2 Physical Formulation

Following the experimental steps described by Le Merrer et al. (2012), we first create numerically a vertical filament of length h and diameter d by stretching a Newtonian fluid of viscosity η located between two parallel pistons and surrounded by air, as illustrated in Fig. 1(a). The filament (yellow part) is then compressed by the pistons (silver parts) that move vertically with a constant velocity $U/2$, inducing fluid deformations (Fig. 1b).

The computational approach used to simulate the filament stretching/compression process is based on a general solver (CIMLIB-CFD, a parallel, finite element library; Coupez and Hachem, 2013) which takes into account the rheological behaviour of each fluid as well as surface tension effects. More precisely, the Cauchy stress tensor $\boldsymbol{\sigma}_c$ is defined as

$$\boldsymbol{\sigma}_c = -p\mathbf{I} + \boldsymbol{\tau}, \quad (1)$$

where, p is the pressure, \mathbf{I} denotes the identity tensor and $\boldsymbol{\tau}$ the *extra stress tensor*. The extra stress tensor is given by

$$\boldsymbol{\tau} = 2\eta\mathbf{D}(\mathbf{u}), \quad (2)$$

$\mathbf{D}(\mathbf{u})$ representing the strain rate tensor and \mathbf{u} the velocity vector. The effective viscosity η is computed by using the power-law constitutive model. The latter includes the Papanastasiou regularization (Papanastasiou, 1987):

$$\eta = k\dot{\gamma}^{(m-1)} \left(1 - e^{-n\dot{\gamma}}\right), \quad (3)$$

where k is the flow consistency index, m denotes the flow behaviour index, $\dot{\gamma}$ represents the second invariant of the strain rate tensor (Bird et al., 1987)

and n is the Papanastasiou coefficient that allows to bound the value of the effective viscosity for vanishing $\dot{\gamma}$.

Our numerical methods are based on a [Variational Multi-Scale](#) (VMS) approach combined with anisotropic mesh adaptation with highly stretched elements (black lines in Fig. 1a), as presented by (Riber et al., 2016).

In order to capture the fluid/air, fluid/pistons and pistons/air interfaces as a function of time, t , a level-set method, which enables the localization and the capturing of interfaces has been used (Hachem et al., 2016). [As described in details in the following section](#), a level-set function is a signed distance function from each interface that is advected with the computed velocity. Velocity and pressure fields are primitive unknowns that are computed using a unified framework, where all fluids occupy a single computational mesh, by simply mixing the different fluid properties (viscosity, density, etc.) using smoothed Heaviside functions (built from each level-set function) to take property discontinuities into consideration.

In the framework presented above, adding surface tension stresses required a specific treatment. The Continuum Surface Force (CSF) method (Brackbill et al., 1992), which enables avoiding the computation of surface integrals by means of a regularized Dirac function, is used. The corresponding momentum equations reads:

$$\rho \left(\frac{\partial \mathbf{u}}{\partial t} + \mathbf{u} \cdot \nabla \mathbf{u} - \mathbf{g} \right) = -\nabla p + \nabla \cdot \boldsymbol{\tau} + \mathbf{f}_{st}, \quad (4)$$

in which ρ , ∇ , \mathbf{g} , $\nabla \cdot$ and \mathbf{f}_{st} are, respectively, the fluid density, the gradient operator, the gravity vector, the divergence operator, and a capillary term

related to the surface tension force, the latter being defined as:

$$\mathbf{f}_{st} = -\sigma K \Phi(\Gamma) \mathbf{n}, \quad (5)$$

where σ , K , $\Phi(\Gamma)$ and \mathbf{n} are the fluid surface tension with air, the curvature of its interface with air, the Dirac function locating the interface Γ , and its normal vector, respectively. Recall that the use of a CSF method induces a regularized Dirac function over a thickness of $2d_{mesh}$, where d_{mesh} is the refined mesh size at the interface. Further details of the present method are given in Section 3 (see also Khalloufi et al., 2016).

Finally, the solid body motion of the pistons is prescribed by directly assigning velocities to nodes of the grid located inside the pistons and by using a penalty mixing rule on viscosities, piston viscosity being set around to 10^6 times the fluid viscosity (Valette et al., 2009, 2019). In practical terms, the pistons are considered as a highly viscous Newtonian fluid ($= 10^9$ Pa·s). Initial and boundary conditions for the flow equations are, respectively, initial rest and zero normal stress in the air domain and prescribed velocity on pistons domains.

The global method used in this work is illustrated in Fig. 1, where the mesh (composed of approximately 10^6 elements) is depicted, adapted around each interface. The corresponding zero-isovalues for each level-set function are also shown. A wide range of filament fluid properties, filament diameter and length, and compression velocity is considered: $(O)10^1 < \rho < (O)10^3$ kg/m³; $0.6 \leq m \leq 1.6$; $(O)10^0 < \eta < (O)10^3$ Pa·s (which is a spatio-temporal function of $\dot{\gamma}$, as denoted by Eq. 3); $(O)10^{-3} < \sigma < (O)10^{-1}$ N/m; $(O)10^{-5} < d < (O)10^{-3}$ m; $h \sim (O)10^{-3}$ m; and $(O)10^{-4} < U < (O)10^{-1}$ m/s. Lastly, both the air viscosity and the air density are constant and respectively equal to 10^{-5} Pa·s

and 1 kg/m^3 .

3 Level-set method and implicit surface tension

3.1 Level-set method

The level-set method enables the localization of the interface between two phases. It consists of a signed distance function widely used in different scientific fields (Osher and Fedkiw, 2003), the definition of which follows. Let Ω denote the whole domain, Ω_l the liquid part and Ω_g the gas part. The level-set function, α , is a signed distance related to the interface $\Gamma = \Omega_l \cap \Omega_g$ and defined at each node X of Ω as:

$$\alpha(X) = \begin{cases} -\text{dist}(X, \Gamma), & \text{if } X \in \Omega_l \\ 0, & \text{if } X \in \Gamma \\ \text{dist}(X, \Gamma), & \text{if } X \in \Omega_g. \end{cases} \quad (6)$$

The time-space evolution of the level-set function is described by the following transport equation (Sussman et al., 1994):

$$\frac{\partial \alpha}{\partial t} + \mathbf{u} \cdot \nabla \alpha = 0. \quad (7)$$

As a distance function, the level-set verifies $\|\nabla \alpha\| = 1$. However, when the interface is convected by a given velocity, the level-set can lose this property and needs to be reinitialized to recover it. A common way to do so is to solve the following Hamilton–Jacobi equation (Sussman et al., 1994):

$$\frac{\partial \alpha}{\partial t_p} + s(\alpha) (\|\nabla \alpha\| - 1) = 0, \quad (8)$$

where t_p is a pseudo-time, and $s(\alpha)$ is the sign function of α . The steady state solution of this non-linear hyperbolic equation will be a distance function from the interface while keeping the zero iso-value unchanged. Following the lines detailed by Coupez et al. (2015), we propose to filter the level-set function in the vicinity of the interface, and thus reducing the computational cost and ensuring mass conservation (Bonito et al., 2016). It consists first in truncating the level-set function using the following expression:

$$\tilde{\alpha} = E \tanh\left(\frac{\alpha}{E}\right), \quad (9)$$

in which E is the thickness of the truncation. The truncated level-set now verifies:

$$\|\nabla\tilde{\alpha}\| = 1 - \left(\frac{\tilde{\alpha}}{E}\right)^2. \quad (10)$$

In the following lines of this section, we simplify the notations by dropping the tilde and assuming that α denotes the truncated level-set function. Lastly, combining both Eqs. (7) and (8), we find the auto-reinitialization level-set equation (see also Bonito et al., 2016):

$$\frac{\partial\alpha}{\partial t} + \mathbf{u} \cdot \nabla\alpha + \lambda s(\alpha) \left[\|\nabla\alpha\| - \left(1 - \left(\frac{\alpha}{E}\right)^2\right) \right] = 0, \quad (11)$$

where λ is a constant proportional to a velocity (see Bonito et al., 2016, for more details). The classical Streamline Upwind Petrov–Galerkin (SUPG) method is used to solve Eq. (11) for its ability to control the spurious oscillations in the convection-dominated regime. Supplemental details are provided in Kallel et al. (2015). Initial and boundary conditions for the fluid level-set equation are, respectively, the initial domain descriptions (as illustrated in figure 1a) and a constant value of E at the domain boundaries. Additionally, initial conditions for the pistons level-set equation are the initial domain descriptions (as show in figure 1a). The values at the domain boundaries are

then kept constant in time.

3.2 Implicit surface tension

As presented in Section 2, a common way to introduce the surface tension as a volume source term in the momentum equations involves rewriting the surface force as $\mathbf{f}_{st} = -\sigma K \Phi(\Gamma) \mathbf{n}$ (Eq. 5). Moreover, the use of a level-set function enables the direct computation of the normal vector as $\mathbf{n} = \nabla\alpha / \|\nabla\alpha\|$ and the mean curvature as $K = -\nabla \cdot \mathbf{n}$. Consequently, the surface tension is expressed as a function of the level-set:

$$-\sigma K \Phi(\Gamma) \mathbf{n} = \sigma \Phi^\epsilon(\alpha) \left[\nabla \cdot \frac{\nabla\alpha}{\|\nabla\alpha\|} \right], \quad (12)$$

where $\Phi^\epsilon(\alpha)$ is a smoothed Dirac function (van der Pijl et al., 2005). According to Hysing (2006), this implementation imposes a restriction on the time step that must respect the propagation of the capillary wave $\frac{c_\sigma \Delta t}{\Delta x} < \frac{1}{2}$, in which $c_\sigma = \sqrt{\sigma\kappa/2\bar{\rho}}$ is the capillary wave phase velocity, $\bar{\rho}$ is the average density at the interface and Δx denotes the mesh size. Taking into account the maximum wave-number $\kappa = \pi/\Delta x$, the time step is restricted to $\Delta t < (\Delta x)^{3/2} \sqrt{\frac{\bar{\rho}}{2\pi\sigma}}$.

In addition, it is stated by Buscaglia and Ausas (2011) that the surface Laplacian of an identity mapping function can be expressed according to the curvature and the normal vector to this interface:

$$\Delta_s \mathbf{I}_\Gamma = \nabla_s \cdot \nabla_s \mathbf{I}_\Gamma = K \mathbf{n}. \quad (13)$$

Following Hysing (2006), we represent the evolution of the position of the interface in time:

$$\mathbf{I}_\Gamma^{o+1} = \mathbf{I}_\Gamma^o + \Delta t \mathbf{u}^{o+1}, \quad (14)$$

where the index $o + 1$ is the current time and o the previous one. Applying the surface Laplacian operator Δ_s on Eq. (14) leads to:

$$-(K\mathbf{n})^{o+1} = -(K\mathbf{n})^o + \Delta t \left(\Delta_s \mathbf{u}^{o+1} \right). \quad (15)$$

Multiplying Eq. (15) by the surface tension and dropping the exponent o in the following lines for simplicity:

$$-\sigma (K\mathbf{n})^{o+1} = -\sigma (K\mathbf{n}) + \sigma \Delta t \left(\Delta_s \mathbf{u}^{o+1} \right). \quad (16)$$

In Eq. (16), we find that the surface Laplacian Δ_s can be expressed in terms of the standard Laplacian as follows:

$$\Delta_s \mathbf{u} = \nabla_s^2 \mathbf{u} = \nabla^2 \mathbf{u} - \frac{\partial^2 \mathbf{u}}{\partial \mathbf{n}^2} - K \frac{\partial \mathbf{u}}{\partial \mathbf{n}}, \quad (17)$$

in which $\frac{\partial \mathbf{u}}{\partial \mathbf{n}} = \nabla \cdot \mathbf{n}$. Therefore, the new surface tension force equation finally reads:

$$\mathbf{f}_{st} = -\sigma K \Phi(\alpha) \mathbf{n} - \sigma \Phi(\alpha) \Delta t \left(\frac{\partial^2 \mathbf{u}}{\partial \mathbf{n}^2} + K \frac{\partial \mathbf{u}}{\partial \mathbf{n}} - \nabla^2 \mathbf{u}^{o+1} \right). \quad (18)$$

The usual term $-\sigma K \Phi(\alpha) \mathbf{n}$ is thus completed by additional terms proportional to the time step that act as an isotropic diffusion minus a diffusion in the normal direction of the interface (Xu and Zhao, 2003). It is also important to emphasise that when the time step tends to zero, the surface tension is defined only by the usual term $-\sigma K \Phi(\alpha) \mathbf{n}$ and, therefore, we retrieve the explicit treatment.

4 Results and Discussion

As previously reported by Le Merrer et al. (2012), under both low gravity (the Laplace pressure, $2\sigma/d$, exceeds the hydrostatic pressure, $\rho gh/2$) and low

inertia ($\text{Re} \ll 1$, where the Reynolds number is $\text{Re} = \frac{\rho U^2}{k(U/h)^m}$) conditions, non-slender Newtonian fluid columns are geometrically stable. In consequence, no deflection, δ , is observed for $d/h > 0.1$ (the deflection condition being defined here as $\delta > d$). This observation is also valid for power-law fluids, as it will be discussed later. Furthermore, two deformation regimes are identified for slender power-law filaments ($d/h \leq 0.1$): a first one driven by the capillary force and during which there is no deflection; and a folding regime dominated by the compressive viscous force. Therefore, the transition between these two regimes can be analysed in the light of a capillary–viscous competition, i.e. the capillary number, Ca (where $\text{Ca} = \frac{k(U/h)^m}{\sigma/h}$).

The two scenarios mentioned above are observed in Fig. 2 that illustrates the compression of non-Newtonian filaments (blue parts) at a constant velocity, U , by two parallel pistons (silver part) for two flow behaviour indexes: $m = 0.8$ (Figs. 2a and 2b; pseudoplastic or *shear-thinning* fluid) and $m = 1.2$ (Figs. 2c and 2d; dilatant or *shear-thickening* fluid). At $\text{Ca} = 1.3$, the *shear-thinning* filament (Fig. 2a) is dominated by the capillary force, which prevents the deflection during the compression. This stabilising effect vanishes at $\text{Ca} = 13$ (Fig. 2b) since the cost of compression becomes greater than the energy related to the folding deformation, which is in turn driven by the viscous force. It is worth noting, however, that no deflection is observed for the *shear-thickening* fluid at $\text{Ca} = 13$ (Fig. 2c). Comparisons between Figs. 2(b) and 2(c) reveal then that the introduction of dilatant effects can stabilise compressed fluid filaments. Nevertheless, once again, an increase of Ca favours the deflection and, consequently, at $\text{Ca} = 47$, the *shear-thickening* filament buckles (Fig. 2d).

The time evolution of the off-z-axis deflection of the centreline for nine non-Newtonian filaments is displayed in Fig. 3. Three different flow behaviour indexes are considered: $m = 0.6$ (Fig. 3a), $m = 0.8$ (Fig. 3b), and $m = 1.2$ (Fig. 3c). For the first material, the buckling is only observed for capillary numbers greater than 0.7 (blue triangles and red diamonds). During the very first instants that follow the beginning of the compression, the thread remains anti-symmetric ($\delta(t) \approx 0$). Nevertheless, after a certain delay, the deflection starts to increase, varying, initially, exponentially, $\frac{\delta}{d} \propto \frac{d^2}{hU}$ (or, simply $\delta(t) \propto e^{\frac{t}{d^2/h}}$), and then with the square root of time, $\delta(t) \propto \sqrt{t - t_0}$ (where t represents time and t_0 denotes the instant from which the deflection develops following a square root time dependence; solid lines). The initial exponential growth of $\delta(t)$ for small deflections ($\delta < d$) can be deduced from the internal–external moment balance described by Euler’s Buckling Theory for elastic solids (Euler, 1744; Timoshenko and Gere, 1963), and later revisited by Le Merrer et al. (2012) for Newtonian fluids. In addition, as shown by the latter authors, the parabolic part of $\delta(t)$ is a direct geometrical consequence of the conservation of filament length after t_0 (or, when $\delta > d$). Here, despite the non-Newtonian nature of material viscosity, both exponential and parabolic parts of $\delta(t)$ are observed, which is theoretically consistent.

Similar to Fig. 2, Fig. 3 also indicates that the critical capillary number from which $\delta(t)$ is greater than d , Ca_c (transition from the capillary to the viscous-dominated regime), is an increasing function of m . At $m = 0.6$ (Fig. 3a), for instance, the filaments are allowed to fold for $\text{Ca} > 0.7$, a picture that does not hold true at $m = 0.8$ (Fig. 3b), since these filaments are stable if $\text{Ca} \leq 1.3$. The stabilising effect of the flow behaviour index is even more pronounced at $m = 1.2$ (Fig. 3c), material whose $\text{Ca}_c \approx 13$. In fact, as shown in Fig.

4(b), Ca_c appears as an increasing power-law function of m : $\text{Ca}_c = k_c^{(3m-2)}$, where $k_c = 5$. This rheological effect on Ca_c seems universal. However, further investigations concerning its physical interpretation are necessary.

It is worth noting that the equation that describes the exponential variation of $\delta(t)$ observed at the beginning of the folding process also represents a characteristic time scale t_{ch} , $\frac{\delta}{\dot{\delta}} \propto \frac{d^2}{hU} = t_{ch}$. The exponential solution of this differential equation ($\delta(t)/\delta_{ch} \sim e^{\frac{t}{t_{ch}}}$, with δ_{ch} denoting the initial deflection at the very beginning (exponential displacement)) was used to construct the dotted lines in Fig. 3. It can be additionally used to estimate the instant from which bending is dominated by the stretching (for $\delta(t) \geq d$), since $t/t_{ch} \sim \ln(d(t)/\delta_{ch})$. In experimental scenarios, the deflection is triggered by thermal perturbations whose order of magnitude is $\delta_{ch} \sim 1$ nm (Le Merrer et al., 2012). In our simulations, however, this process is started by numerical instabilities related to the mesh size. Taking the scale of our smaller mesh element for δ_{ch} , $d/\delta_{ch} \sim (O)10^3$. Consequently, $t/t_{ch} \approx 10$ when $\delta(t) = d$. Later on, for $t > 10\frac{d^2}{hU}$ and $\delta > d$, the square root time-dependent growth of the deflection takes place, as exposed previously. In other words, $t_0 > 10\frac{d^2}{hU}$ (or, simply $t_0 > 10t_{ch}$).

The buckling time condition discussed above is confirmed by Fig. 4(a) in which t_0 is plotted against $t_{ch} = \frac{d^2}{hU}$ for 300 different cases (each point representing a numerical simulation) and four different flow behaviour indexes: $m = 0.6$ (grey circles; *shear-thinning*), $m = 0.8$ (blue triangles; *shear-thinning*), $m = 1.0$ (red diamonds; Newtonian), and $m = 1.2$ (green squares; *shear-thickening*). Our data collapse on a single linear curve of slope 61.7 (black solid line; $t_0 = 61.7t_{ch}$). Moreover, Fig. 4(a) indicates that, irrespective of the regime, slender bodies tend to buckle earlier (which is also shown in Fig. 3).

It is worth noting that, since buckling can only be observed if t_0 is smaller than the numeric experiment duration, h/U , a deflection criterion for the folding regimes can be developed as follows:

$$t_0 = k_0 t_{ch} < \frac{h}{U}, \quad (19)$$

where k_0 indicates a constant equal to 61.7. Then,

$$k_0 \frac{d^2}{hU} < \frac{h}{U}, \quad (20)$$

and, in consequence,

$$\frac{d}{h} < \frac{1}{\sqrt{k_0}}. \quad (21)$$

This leads to a geometrical criterion according to which the maximum value of d/h related to the folding regime is on the order of $(O)10^{-1}$. Hence, only slender enough filaments are likely to buckle. Effectively, our results indicate that the folding regime is observed only when d/h is smaller than 0.1.

Both the force ratio ($\text{Ca} > k_c^{(3m-2)}$) and the geometrical ($d/h < 0.1$) criteria for the folding regime found along the present work are in excellent agreement with the almost 500 numerical results displayed by Fig. 5. In this figure composed of four sub-figures (5a, 5b, 5c, and 5d), each point corresponds to a simulation. Additionally, each sub-figure is related to a specific flow behaviour index: $m = 0.6$ (5a; *shear-thinning*); $m = 0.8$ (5b; *shear-thinning*); $m = 1.0$ (5c; *Newtonian*); $m = 1.2$ (5d; *shear-thickening*). In these sub-figures, we report whether there is folding (blue triangles) or no deflection (grey circles). For each m , the results are summarised in a two-dimensional phase diagram, whose axes are the slenderness parameter (d/h) and the capillary number (Ca). Within the grey region, the fluid filaments are not allowed to buckle due to their morphology ($d/h > 0.1$). Regarding the slender filaments ($d/h < 0.1$),

however, the folding regime driven by the compressive viscous force is reached when $\text{Ca} > 5^{(3m-2)}$. Below this value, the compressed filament is dominated by the capillary force and, consequently, the folding does not develop. Finally, it is important to emphasise that the Newtonian diagram displayed by Fig. 5(c) is perfectly in line with the experimental results previously reported by Le Merrer et al. (2012).

5 Concluding Remarks

Following the development of an adaptive variational multi-scale method for three materials (air, non-Newtonian fluid, and pistons) with surface tension, we analysed through direct numerical simulations and scaling laws the buckling of filaments of power-law fluids compressed at constant velocity by two parallel pistons. A level-set function was used to provide a precise position of the interfaces.

In short, under both low gravity ($\frac{2\sigma}{d} > \frac{\rho gh}{2}$) and low inertia ($\text{Re} \ll 1$) conditions, two compression regimes were observed for slender filaments ($d/h < 0.1$): a first one driven by the capillary force and during which there is no deflection; and a second folding regime that is dominated by the compressive viscous force. Noticeably, there is a strong analogy between viscous and elastic buckling, since both phenomena are observed when rapidly compressing enough slender filaments. In addition, interestingly, the critical capillary number related to the transition between the deformation regimes mentioned above appears as an increasing function of the flow behaviour index, $\text{Ca}_c = 5^{(3m-2)}$.

It would be interesting to consider in future works the gravity and inertial effects on the buckling of slender fluid filaments, as well as those related to

other non-Newtonian entities (such as the yield-stress).

Acknowledgements

We would like to express our sincere gratitude to PSL Research University for their support under the program ‘Investissements d’Avenir’ launched by the French Government and implemented by the French National Research Agency (ANR) with the reference ANR-10-IDEX-0001-02 PSL.

References

- Barnes, G., Woodcock, R., 1958. Liquid rope-coil effect. *American Journal of Physics* 26, 205–209.
- Bird, R.B., Armstrong, R.C., Hassager, O., 1987. *Dynamics of polymeric liquids*. Wiley-Interscience, New York 2nd edition, 172–173.
- Bonito, A., Guermond, J.L., Lee, S., 2016. Numerical simulations of bouncing jets. *International Journal for Numerical Methods in Fluids* 80, 53–75.
- Brackbill, J., Kothe, D., Zemach, C., 1992. A continuum method for modeling surface tension. *Journal of Computational Physics* 100(2), 335–354.
- Buscaglia, G.C., Ausas, R., 2011. Variational formulations for surface tension, capillarity and wetting. *Computer Methods in Applied Mechanics and Engineering* 200, 3011–3025.
- Coupez, T., Hachem, E., 2013. Solution of high-Reynolds incompressible flow with stabilized finite element and adaptive anisotropic meshing. *Computer Methods in Applied Mechanics and Engineering* 267, 65–85.
- Coupez, T., Silva, L., Hachem, E., 2015. Implicit boundary and adaptive

- anisotropic meshing. *New Challenges in Grid Generation and Adaptivity For Scientific Computing*, Springer International Publishing 5, 1–18.
- Cruickshank, J.O., 1988. Low-Reynolds-number instabilities in stagnating jet flows. *Journal of Fluid Mechanics* 193, 111–127.
- Euler, L., 1744. *Methodus inveniendi lineas curvas maximi minimive proprietate gaudentes, Additamentum I (de curvis elasticis)*. Leonardi Euleri Opera Omnia 24, 245.
- Griffiths, R.W., Turner, J.S., 1988. Folding of viscous plumes impinging on a density or viscosity interface. *Geophysical Journal International* 95, 397–419.
- Habibi, M., Hosseini, S.H., Khatami, M.H., Ribe, N.M., 2014. Liquid supercoiling. *Physics of Fluids* 26, 024101–1–024101–11.
- Hachem, E., Khalloufi, M., Bruchon, J., Valette, R., Mesri, Y., 2016. Unified adaptive variational multiscale method for two phase compressible and incompressible flows. *Computer Methods in Applied Mechanics and Engineering* 308, 238–255.
- Hysing, S., 2006. A new implicit surface tension implementation for interfacial flows. *International Journal for Numerical Methods in Fluids* 51, 659–672.
- Johnson, A.M., Fletcher, R.C., 1994. *Folding of viscous layers: Mechanical analysis and interpretation of structures in deformed rock*. Columbia University, New York .
- Kallel, A., Hachem, E., Rapetti, F., Demay, Y., Agassant, J.F., 2015. Stability analysis of a polymer film casting problem. *International Journal for Numerical Methods in Fluids* 78, 436–454.
- Khalloufi, M., Mesri, Y., Valette, R., Massoni, E., Hachem, E., 2016. High fidelity anisotropic adaptive variational multiscale method for multiphase flows with surface tension. *Computer Methods in Applied Mechanics and*

- Engineering 307, 44–67.
- Le Merrer, M., Quéré, D., Clanet, C., 2012. Buckling of viscous filaments of a fluid under compression stresses. *Physical Review Letters* 109, 064502.
- Mahadevan, L., Ryu, W.S., Samuel, A.D.T., 1998. Fluid 'rope trick' investigated. *Nature* 392, 140.
- Mahadevan, L., Ryu, W.S., Samuel, A.D.T., 2000. Correction: Fluid 'rope trick' investigated. *Nature* 403, 502.
- Osher, S., Fedkiw, R., 2003. *Level set methods and dynamic implicit surfaces*. Springer 19.
- Ostwald, W., 1925. Ueber die geschwindigkeitsfunktion der viskosität disperser systeme. *Kolloid-Z* 36, 99–117.
- Papanastasiou, T., 1987. Flows of materials with yield. *Journal of Rheology* 31, 385–404.
- Pearson, J., 1985. *Mechanics of polymer processing*. Elsevier, Amsterdam .
- Pilkington, L.A.B., 1969. Review lecture: The float glass process. *Transport Phenomena and Fluid Mechanics*, *AIChE Journal* 314, 1–25.
- Ribe, N.M., 2003. Periodic folding of viscous sheets. *Physical Review E* 68, 036305–1–036305–6.
- Ribe, N.M., 2017. Liquid rope coiling: a synoptic view. *Journal of Fluid Mechanics* 812, R2.
- Ribe, N.M., Habibi, M., Bonn, D., 2012. Liquid rope coiling. *Annual Review of Fluid Mechanics* 44, 249–266.
- Ribe, N.M., Huppert, H.E., Hallworth, M.A., Habibi, M., Bonn, D., 2006. Multiple coexisting states of liquid rope coiling. *Journal of Fluid Mechanics* 555, 275–297.
- Riber, S., Valette, R., Mesri, Y., Hachem, E., 2016. Adaptive variational multiscale method for Bingham flows. *Computers and Fluids* 138, 51–60.

- Sussman, M., Smereka, P., Osher, S., 1994. A level set approach for computing solutions to incompressible two-phase flow. *Journal of Computational Physics* 114, 146–159.
- Taylor, G.I., 1969. *Proceedings of the Twelfth International Congress of Applied Mechanics*, Stanford, 1968 Springer-Verlag, Berlin, 382.
- Timoshenko, S.P., Gere, J.M., 1963. *Theory of elastic stability*. McGraw-Hill, New York .
- Tomé, M.F., Araujo, M.T., Evans, J., Mckee, S., 2019. Numerical solution of the giesekus model for incompressible free surface flows without solvent viscosity. *Journal of Non-Newtonian Fluid Mechanics* 263, 104–119.
- Valette, R., Coupez, T., David, C., Vergnes, B., 2009. A direct 3D numerical simulation code for extrusion and mixing processes. *International Polymer Processing* 24, 141–147.
- Valette, R., Hachem, E., Khalloufia, M., Pereira, A.S., Mackley, M.R., Butler, S.A., 2019. The effect of viscosity, yield stress, and surface tension on the deformation and breakup profiles of fluid filaments stretched at very high velocities. *Journal of Non-Newtonian Fluid Mechanics* 263, 130–139.
- van der Pijl, S.P., Segal, A., Vuik, C., Wesseling, P., 2005. A mass-conserving level-set method for modelling of multi-phase flows. *International Journal for Numerical Methods in Fluids* 47, 339–361.
- Xu, J.J., Zhao, H.K., 2003. An eulerian formulation for solving partial differential equations along a moving interface. *Journal of Scientific Computing* 19, 573–594.
- Yarin, A.L., Tchavdarov, B.M., 1996. Onset of folding in plane liquid films. *Journal of Fluid Mechanics* 307, 85–99.

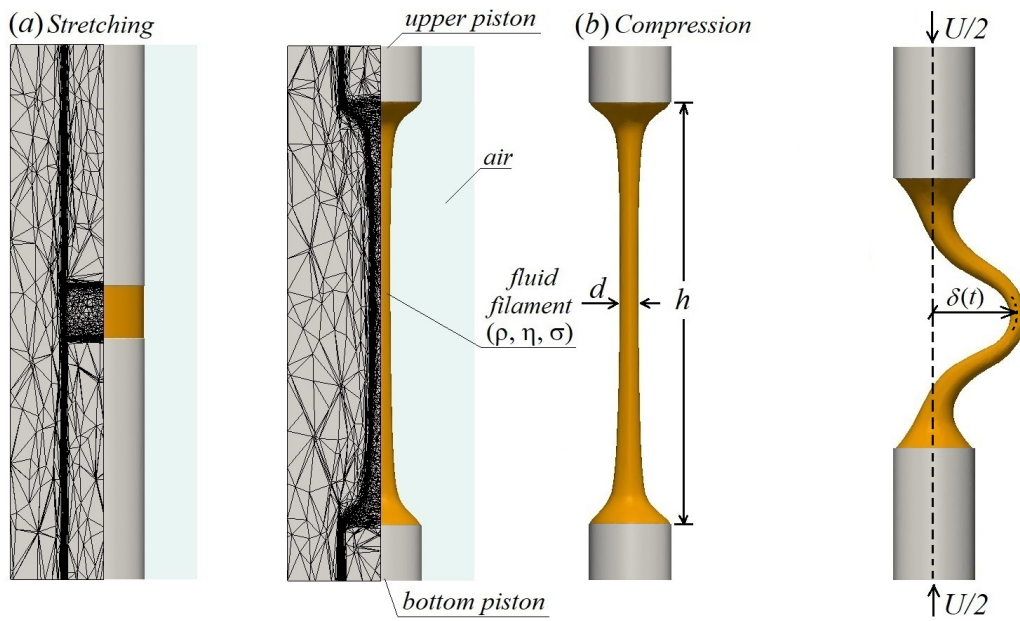


Fig. 1. (a/b) Stretching/compression of a fluid filament. Left in (a): adapted mesh ($\approx 10^6$ elements) of the computational domain. Right in (a), and (b): zero iso-values of pistons and fluid level-set functions.

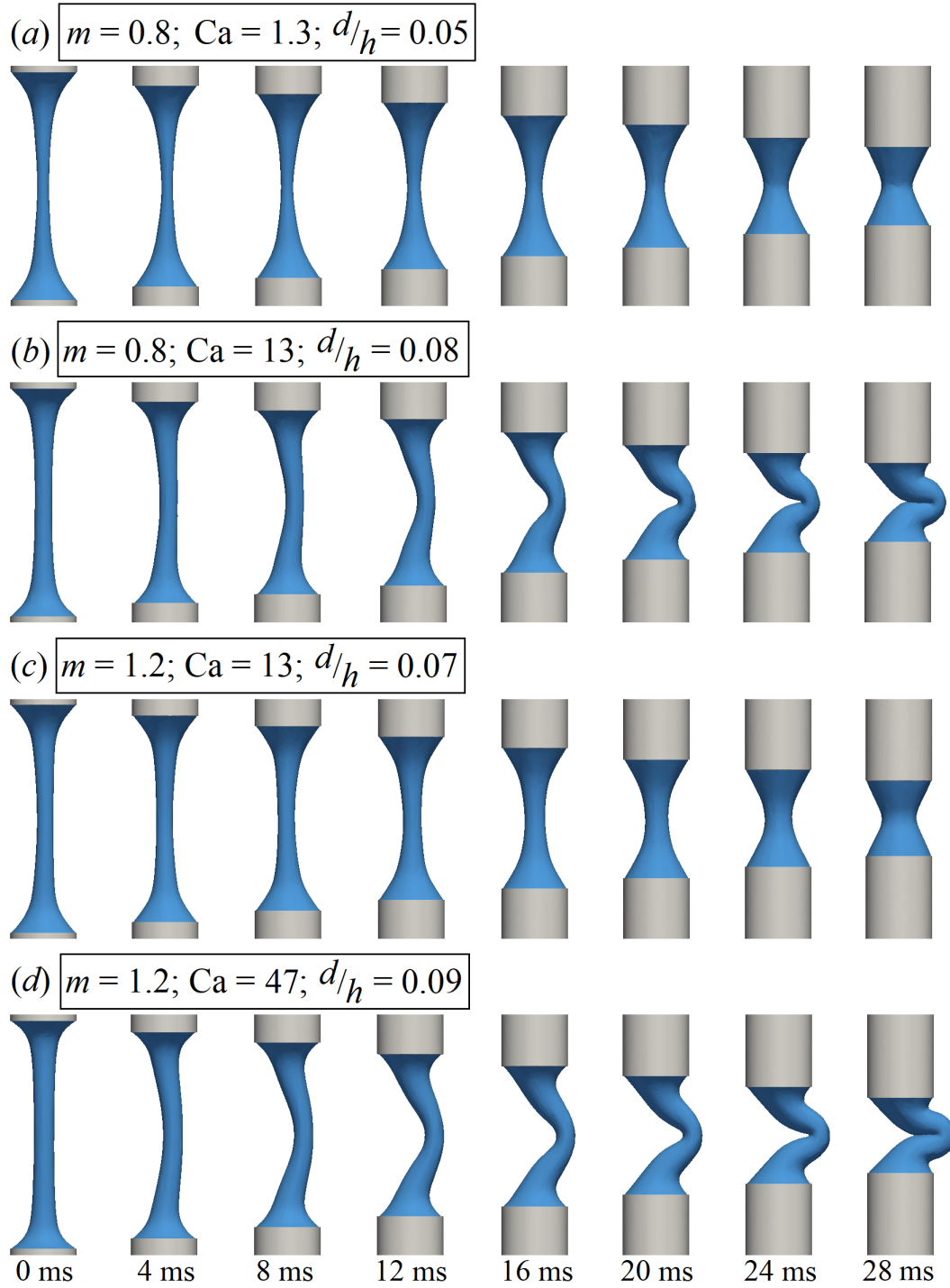


Fig. 2. Compression of power-law fluid filaments (blue part) at a constant velocity, U , by two parallel pistons (silver parts). Capillary-dominated (*a* and *c*) and viscous-dominated (*b* and *d*) compression cases are displayed at eight different instants ($0 \text{ ms} \leq t \leq 28 \text{ ms}$) for two flow behaviour indexes: $m = 0.8$ (*a* and *b*) and $m = 1.2$ (*c* and *d*).

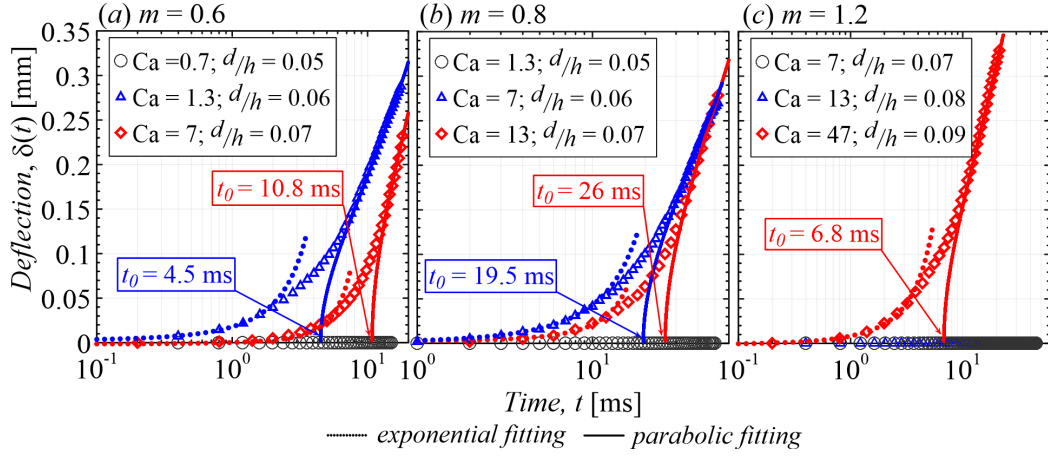


Fig. 3. Time evolution of the off-axis deflection, $\delta(t)$, of the centreline of nine non-Newtonian filaments. The deflections curves related to the folding regime are divided into two parts: exponential (dotted line; $\delta(t) \propto e^{\frac{t}{d^2/Uh}}$) and parabolic (solid line; $\delta(t) \propto \sqrt{t - t_0}$ (solid lines)). Three different flow behaviour indexes are taken into account: $m = 0.6$ (a), $m = 0.8$ (b), and $m = 1.2$ (c).

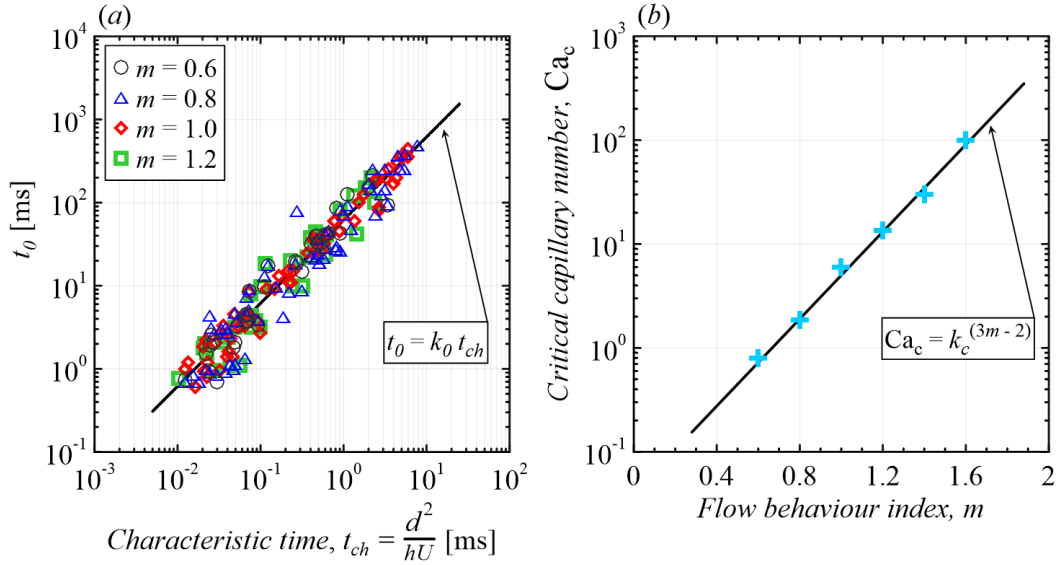


Fig. 4. (a) Starting time of the viscous buckling, t_0 , against the buckling characteristic time, t_{ch} , for 300 different cases (each point representing a numerical simulation). (b) Critical capillary number, Ca_c , as a function of the flow behaviour index, m .

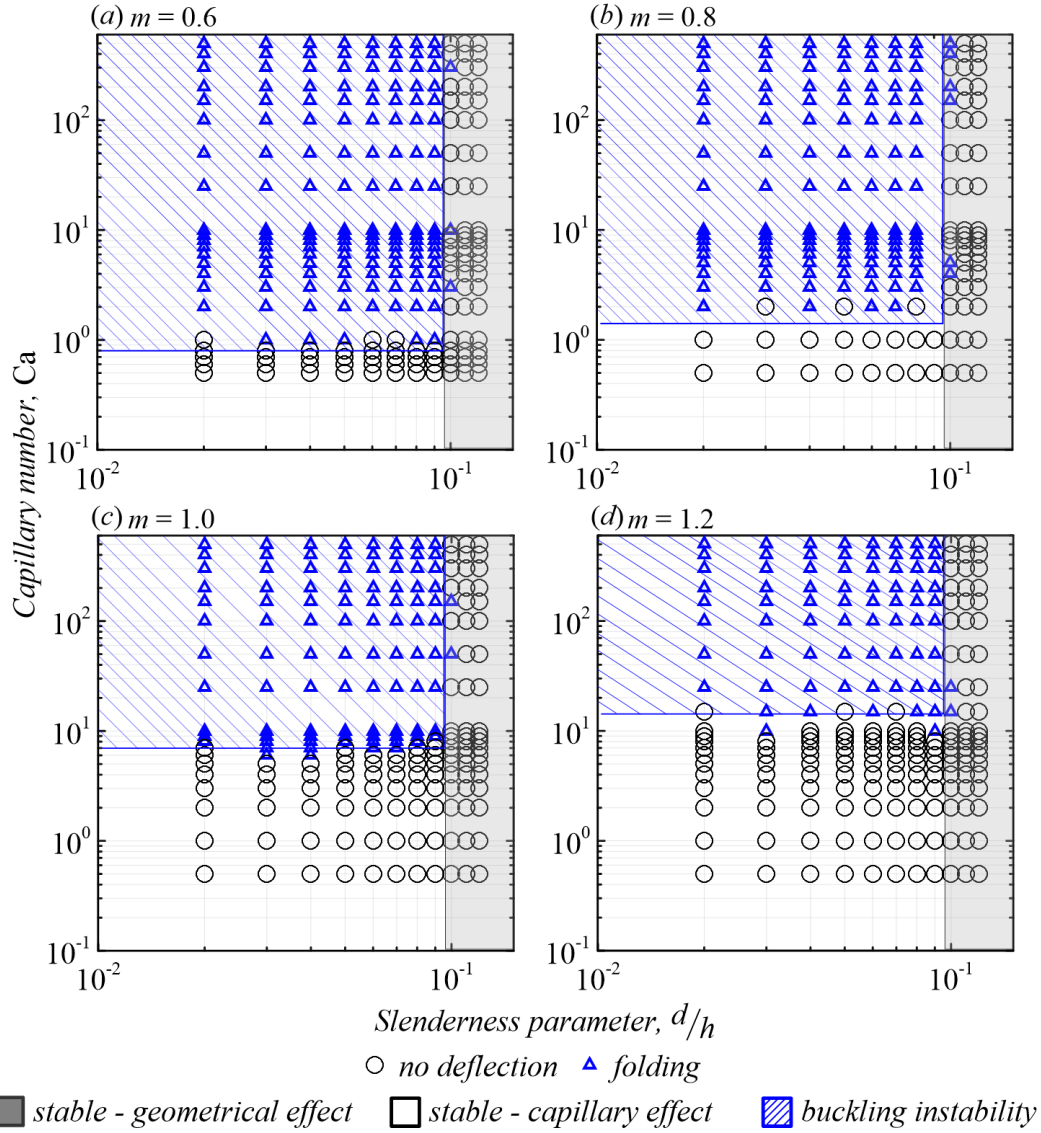


Fig. 5. Ca - d/h diagram for four different m : 0.6 (*a*, shear-thinning), 0.8 (*b*, shear-thinning), 1.0 (*c*, Newtonian), and 1.2 (*d*, shear-thickening). In these four sub-figures, we report whether there is folding (blue triangles) or no deflection (grey circles). Each point corresponds to a simulation. [Almost 500 numerical results are taken into account.](#) Both the grey and the white regions represent deformation regimes for which no deflection is observed do to the stabilising effects of d/h and σ , respectively. The blue hatched region indicates the folding regime.